An automated testing machine for monitoring the evolution of fiber breaks

G. A. Holmes · Sheldon Wesson · W. G. McDonough · J. H. Kim · A. Netravali · J. N. Walker · R. A. Johnson

Abstract A cooperative agreement between the National Institute of Standards and Technology (NIST) and the Textile Research Institute/Princeton (TRI/Princeton) has resulted in the development of an automated tensile testing machine for determining the interfacial shear strength (IFSS) as determined by the single fiber fragmentation (SFF) test. The imaging capability of this new machine permits the archiving of data for additional analyses as new data reduction methods are developed and provides a framework for the sharing of fragmentation data among researchers. To keep pace with the changing directions of composite micromechanics research, the new machine was extended to obtaining archival data on fiber fragmentation in 2D multifiber arrays by utilizing a new fiber placement device that allows for the precise placement of these arrays within the dogbone specimen.

G. A. Holmes · W. G. McDonough (✉) · J. H. Kim
Polymers Division, Characterization and Methods Development Group, National Institute of Standards and Technology, 100 Bureau Drive Stop 8541, Gaithersburg, MD 20899-8541, USA
e-mail: walter.mcdonough@nist.gov

S. Wesson
TRI/Princeton, 601 Prospect Avenue, Princeton, NJ 08542-4034, USA

A. Netravali
Department of Textiles & Apparel, Cornell University, 201 Martha Van Rensselaer Hall, Ithaca, NY 14853-4401, USA

J. N. Walker
Electrim Corp, 356 Wall Street, Princeton, NJ 08540-1517, USA

R. A. Johnson
Exxon Mobil Research and Engineering, 3225 Gallows Road. Rm. 6A2221, Fairfax, VA 22037-0001, USA

Present Address:
S. Wesson
Adherent Technologies, 11208 Cochiti SE, Albuquerque, Albuquerque, NM 87123, USA

Introduction

Since the early development of polymer composites, adhesion between the matrix and fibers has been known as a critical factor that influences the mechanical properties and performance of composites. Therefore, composite interphase micromechanics evolved as a multidisciplinary research area, with the primary focus being the determination of the interfacial shear strength (IFSS) between the fibers and matrix of composite structures. To accomplish this goal, several test methodologies (the single fiber pullout test, the single fiber fragmentation test, the micro-debond test, and the micro-indentation test) were developed. Of these tests, it is generally accepted that the loading found in the single fiber fragmentation test (SFFT) is consistent with the loading behavior observed in composites.

Holmes et al. [1], however, indicated that the IFSS could be dependent on the testing rate. In that article, the testing rate was based on a sequential step-strain approach utilizing deformation steps of approximately 0.1 mm followed by a 10 min dwell time between strain increments. This procedure was chosen to allow the counting of the number of fiber breaks between strain increments. From these data the in situ fiber strength at the critical transfer length may be estimated. This parameter, which corresponds to the distance required to transfer the stress from the matrix to the fiber, is essential for determining the IFSS from the SFFT.

Because this testing protocol often requires 5–6 h per sample to complete, the usefulness of the SFFT as a standard testing procedure has been questioned. To address this concern, improvements to the SFFT were sought by the National Institute of Standards and Technology (NIST) that increased sample throughput while minimizing the manpower requirements of the SFFT. In 1995, NIST commissioned the development of an automated IFSS testing apparatus through a cooperative agreement with Textile Research Institute (TRI)/Princeton. The major goal for this instrument was to provide a standard testing framework for determining the IFSS at the fiber polymer interphase region. To determine the in situ strength of the fiber at the critical transfer length, an automated machine that collects the relevant data after each strain-step was sought. Therefore, the new machine would require the development of algorithms for recording the image of the specimen at each strain increment and algorithms for the automatic detection of fiber breaks. To facilitate data reduction, the new machine was also required to incorporate the current methodologies for analyzing SFF test data.

Since the SFFT involves the controlled fragmentation of a single fiber, the impact of adjacent fibers on the IFSS and the manner in which critical flaws are nucleated in composites structures are not addressed by this test. To overcome these shortcomings, the experimental micromechanics research community shifted their focus toward the controlled fracture of multifiber arrays [2–13]. This new direction was seen as a way to illuminate the mechanisms involved in critical flaw nucleation in unidirectional composites, while determining the impact of fiber–fiber interactions on the critical transfer length parameter, since these parameters are often used in composite failure models. Therefore, it was reasoned that the usefulness of the automated instrument would be greatly enhanced if the evolution of fiber breaks in multifiber arrays could be monitored and the data archived through images to allow analysis using image processing software. As will be shown, only minor modifications were required to the instrument to accommodate imaging of 2D multifiber arrays. Because methodologies for reducing the data from the multifiber arrays are still being developed, data reduction is still being performed manually. Therefore, this report describes an automated tensile testing apparatus for quantifying the IFSS as measured by the SFF test and archiving the evolution of fiber breaks in multifiber arrays.

Apparatus

The apparatus for automating IFSS measurements consists of five components: a frame/actuator that strains the specimen, a digital camera and microscope lens mounted on a
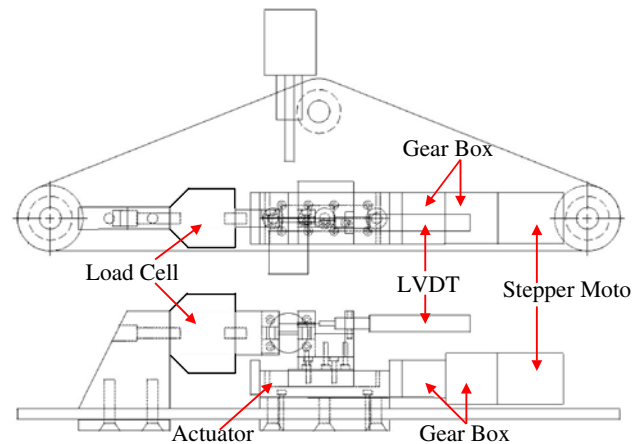

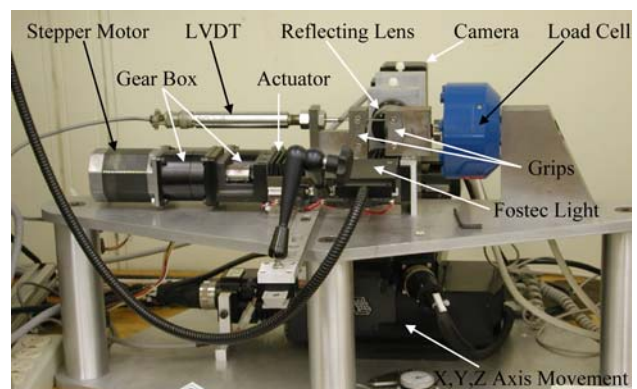Fig. 1 Schematic of interfacial shear strength apparatus

Fig. 2 Automated interfacial shear strength apparatus

three-axis positioner, a computer, a program that conducts the experiment, and a program for measuring break lengths and fragment lengths in the images.

Frame/actuator

A schematic of the apparatus for straining single fiber composites is shown in Fig. 1 and a picture of the machine is shown in Fig. 2. The metal frame for straining the specimen is a THK 3306A-150L-02463 actuator with a 0.6 cm lead screw from Axis Inc.[1] The screw is activated by a Parker Hannifin Compumotor OEM 57–83 stepper motor driven with an OEM 300 power module, controlled with an OEM 650X microstepping drive, and fitted with a Bayside NE 23-100 100:1 gearbox. This system provides a dynamic range of strain rate from 0.15% to 120% min^{-1}

based on a 2 cm gauge length. The maximum sample length of 2.4 cm is established by the 2.5 cm maximum horizontal displacement attainable by the three-axis camera positioner.

Grip displacement is measured with a GCD-121-250 LVDT system featuring a 1.27 cm stroke by Lucas Controls. The signal from the LVDT is oversampled and digitally filtered to provide 1 µm repeatability in grip positioning. The Model 1110AF load cell by Interface Inc. measures 1500 N full scale in tension or compression.

A 16 bit AX-MIO-16X multifunction data acquisition board by National Instruments samples output from the LVDT and load cell at 4 kHz. Two-ended bipolar operation of the board provides 2^{-15} resolution of analog input, which is 10 V full-scale for both instruments. Averages of 100 measurements per sample are written to disk at 10 Hz to record the load curve during specimen elongation.

Optics

An Electrim 1000L camera fitted with an Ealing 25X 25-0514 reflecting objective microscope lens provides a horizontal resolution of 0.8 µm pixel^{-1} and a vertical resolution of 0.3 µm pixel^{-1} (see Fig. 3). The Time Delay and Integration (TDI) image is 753 pixels wide and can be any
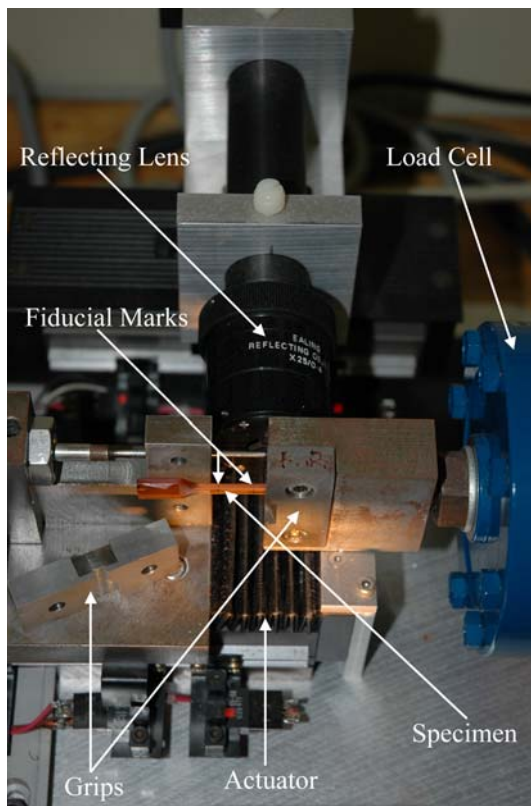

Fig. 3 Automated interfacial shear strength apparatus. Close-up of grip region. Note fiducial marks on the test specimen

length. A complete TDI scan of 2 cm produces TIFF files greater than 20 MB. However, the pixel array in each dimension can be reduced by a factor of 2 to 8 during the scan, thereby reducing the size of the TDI images.

Ealing 53-8009-02 DPS precision stepper stages for the TDI scan and camera focus provides a minimum step length of 0.5 µm over a total traverse of 2.5 cm. TDI velocity, which is fixed for a given magnification and exposure time, is 0.06 cm s^{-1} for this system, well within the dynamic range of 0.001–1.5 cm s^{-1}. A 0.25 µm step size is attained over a total vertical traverse of 1 cm with the Ealing 53-8058 DPS vertical lift unit. This detailed motion control is convenient for finding the fiber and focusing the image.

Computer

The computer is a Dell 100 MHz Pentium system featuring a 256 k secondary cache, 64 MB RAM, an Adaptec 2940 bus mastering PCI SCSI controller, a 230 MB Fujitsu M2512A optical disk and a NEC 6X Multispin CD reader. Graphics are rendered on a 17" Sony CDP-17SF1 monitor with a 64 bit Number Nine GXE64 PCI graphics card with 4 MB VRAM. In its original configuration, the computer was equipped with a 2.1 GB Seagate ST12400 N hard disk and controlled by the Windows 95 operating system. Due to limitations in data storage capacity inherent with the Windows 95 operating systems, the storage capacity was recently increased to 8 GB and the operating systems upgraded to Windows 98. Future upgrades will depend on the compatibility of the software algorithms with later versions of Windows.

IFSS/strain

A program written in LabVIEW from National Instruments controls all aspects of data acquisition. The program comprises several modules:

Panel: In this module system variables and calibration factors are entered (see Fig. 4). In the example shown in the figure, the gauge length of the sample is 1.950 cm, and the grips are programmed to increase by 0.200 cm in 10 strain steps. Since the strain rate of each deformation is set to 0.00050 cm/s, it will take approximately 40 s in this example for each strain step to be completed. The TDI image is scanned for a total of 2.3 cm to ensure that the complete image of the sample gauge length is obtained on each strain step. In the *schedule sub-panel*, the dwell time between strain steps for this example is 4 min and images are taken at the beginning of the test (0), immediately

Fig. 4 Picture of the Panel Module from the IFSS Strain Program, which controls all of the data acquisition parameters
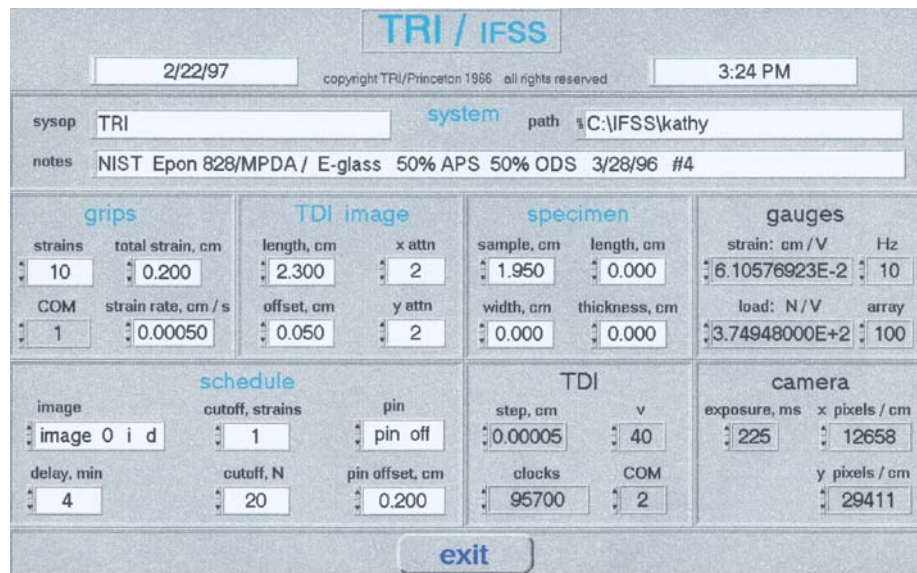
after the strain step (*i*) and immediately before the next strain step (*d*). This imaging protocol was added to quantify how delayed fracture events within a strain step impact critical flaw nucleation (e.g., see Holmes et al. [14]). Because disk space size was limited when this machine was developed, the TDI image is attenuated by a factor of 2 (see *TDI image sub-panel*) to ensure that there was ample space on the disk for the 21 images that will be taken.

Grips: A utility for checking the LVDT and load cell, and for positioning the moving grip. The calibration factors for the LVDT and load cell are given in the *Gauges sub-panel* of the Panel module (see Fig. 4).

Image: Find the fiber and focus; set up the TDI scan.

Strain: Incrementally elongate the specimen then TDI scan. Write the load/displacement curve and TDI image to disk. An example of the images obtained after each step strain is shown in Fig. 5.

Report: Send an image of the control panel to the printer to document experimental conditions.

The program writes a new directory when the Strain module is first activated, using a timestamp as the directory name. Experiment conformation files, load/displacement curves, and TDI images for a given specimen are all written to this directory. Load/displacement files are in ASCII format for convenient importing into other programs for subsequent analysis.

IFSS/count

A program written in LabVIEW for analysis of TDI images consists of two main modules.

Count: Measure fragment lengths and break lengths by finding break centers or break edges with a mouse.

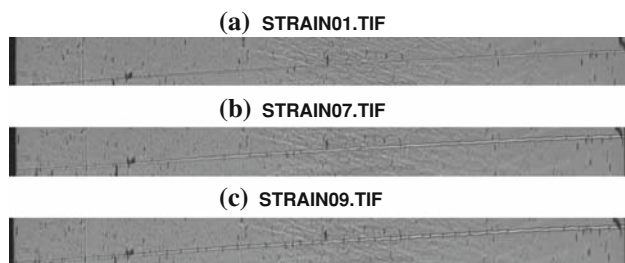Analyze: Experimental routines for automated break finding using image analysis.

Materials and experimental

The single fiber fragmentation data shown in Fig. 6 and the multifiber test specimen shown in Fig. 7 were made with diglycidyl ether of bisphenol-A epoxy resin (DGEBA) (Epon Resin 828 (80% by mass)) and diglycidyl ether of butanediol (DGEBD) (RD-2 (20% by mass)) cured with stoichiometric amounts of *meta*-phenylenediamine (*m*-PDA) using the standard silicon molds discussed previously [1]. The specimens were deformed to 8–10% strain

(a) STRAIN01.TIF

(b) STRAIN07.TIF

(c) STRAIN09.TIF

Fig. 5 TDI images of a single filament composite under elongation. Photo titles indicate the number of 0.01 cm strain increments. Fragmentation is evident in **b** and is complete in **c**. Note that the fiber is canted relative to the horizontal axis of the image
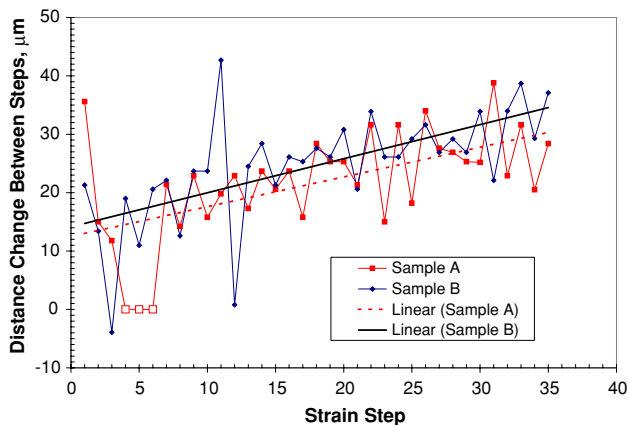
Fig. 6 Distance change between strain steps of two representative test specimens (A and B) deformed in 35 strain increments to 8.1% and 8.2% strain, respectively
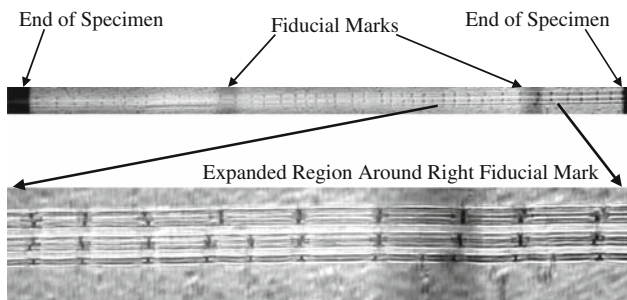

Fig. 7 A typical multifiber array (5 E-glass fibers) with fiducial marks and fragmented

Fig. 8 Typical load–displacement curve for the fragmentation of an epoxy/E-glass single fiber fragmentation specimen

by expanding the grips by a total of 0.3 cm (i.e., from 2.0 cm to 2.3 cm) using 35 strain increments at a strain rate of 0.0085 cm/s with TDI images being obtained after each strain increment.

All other specimens were prepared with DGEBA epoxy resin DER 331 (80% by mass) and diglycidyl ether of polyglycol (DER 736 (20% by mass)) cured with a tre-traethylene pentamine (DEH #26) curing agent (13.3% by mass of total resin) were molded in silicone forms with 20 μm glass filaments. The dimensions of these specimens were 0.3 cm wide and 0.08 cm thick with a gauge length of 1.6 cm. These specimens were elongated in 0.01 cm increments at a strain rate of 3×10^{-4} s^{-1} and TDI images were also obtained after each strain increment.

Representative results

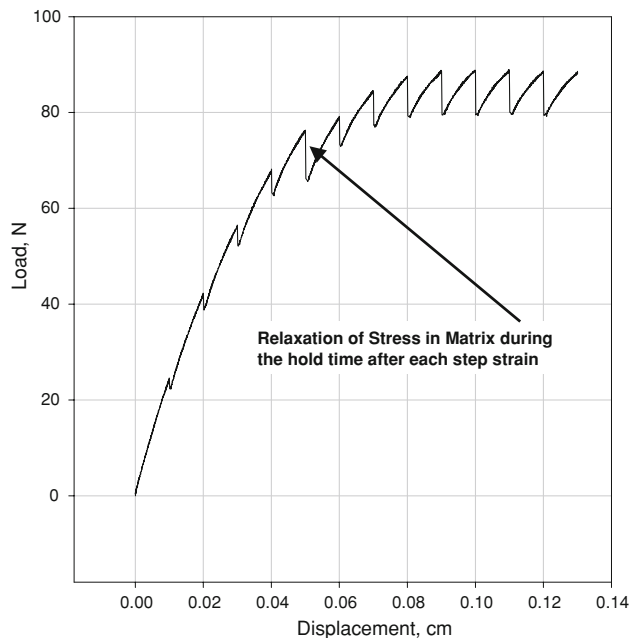Figure 8 shows a typical load displacement curve for a SFF specimen. The drop in load after each strain step is due to stress-relaxation in the viscoelastic matrix with time. This relaxation behavior is consistent with results obtained by Holmes et al. [1] using a manual SFFT apparatus.

In addition to minimizing manpower requirements, another key advantage of automated testing is the ability to reproducibly deform test specimens. In Fig. 6, two specimens were deformed to 8% strain by programming the grips to separate by a total of 0.3 cm (i.e., from 2.0 cm to 2.3 cm) using 35 strain increments at a strain rate of 0.0085 cm/s (see Fig. 4). For this test, the total time for each strain increment was 1 s. However, since the specimen deforms in the grips, an accurate measure of specimen strain can only be obtained from the fiducial marks that are placed on the test specimen gauge section (see Fig. 3). The linear trendlines of the data in Fig. 6 indicates that on average the actual deformation increases from 13–15 μm to 25–30 μm, when the demand on the grips at each strain step is 85 μm. Since the trendlines have similar slopes, this indicates that reproducible deformation profiles are achievable with this instrument.

Representative images of fiber breaks along a single fiber test specimen are shown in Fig. 9. The sharpness of the image is controlled in the *Image panel* of the IFSS/strain program. Since the width of the TDI image is approximately 200 μm, the fiber placement device described in the previous article is essential for obtaining a fiber specimen that remains in the camera's field-of-view and in focus along the 2 cm plus region scanned by the camera. However, even with precise horizontal placement of the fibers, canting (see Fig. 5) and defocusing does occur in the TDI images with successive strain steps. The canting
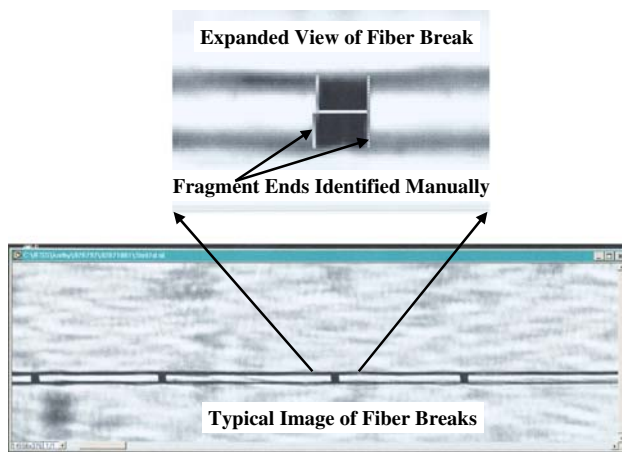
Fig. 9 Typical image of fiber breaks obtained from TDI scan

problem was minimized in this design by adjusting the location of the sample holder region in one of the grips by approximately 40 μm. Since the defocusing occurs slowly, the TDI image must be refocused approximately every 5 strain steps during the data acquisition process. A second-generation design of this instrument by Wesson has eliminated these problems.

Figure 7 shows a typical TDI image from a 2D multi-fiber array that has been tested with the current machine. From this image one can see that the array of fibers is canted from horizontal. Noting the fiducial marks on the specimen image, one can see that the five fibers are in focus and remain in the field of view along the TDI image of the 2 cm gauge section. In this figure a region along the right fiducial mark has been expanded to aid in viewing the spacing between the fibers and the coordinated fracture patterns that occur between these closely spaced fibers.

Automated analysis of fiber breaks

From the previous figures, breaks in E-glass microcomposites manifest themselves as dark regions between fiber ends. These darken region are composed of the two broken fiber ends and an area of debonding interphase region at the fragment ends. A detail discussion of the debonding phenomenon can be found elsewhere [15]. Although this has been the preferred method in this laboratory for detecting fiber breaks, the birefringence pattern that appears under cross-polarized light may also be imaged as a TDI scan and used to detect fracture sites.

The latter approach is useful in the case of carbon fiber microcomposites, since the carbon fibers appear black in a grayscale image, thereby showing little or no contrast with the breaks. In this case, the birefringence must be used to indicate the position of the breaks. On the other hand, if the fiber debonds from the matrix at the interface,

birefringence patterns will be weak and will overlap, showing little or no delineation between fractures. In this case the breaks themselves must be used as objects for classification.

Currently, mathematical functions implemented in the LabVIEW IMAQ Image Analysis Library are used to locate and report fiber fractures in a single fiber composite specimen automatically. A flowchart of the process is presented in Fig. 10.

After an image is delivered to the algorithm, histogram stretching is used to enhance contrast. The image is then threshold to highlight regions of interest, which in this case are either breaks or birefringence caused by the breaks. The threshold operation is performed automatically by either the clustering method (to detect breaks) or the entropy method (to find birefringence patterns). The result of this process is a binary image with white regions (pixel value of 255) corresponding to the regions of interest on a black background (pixel value of 0).

If the image displays birefringence, patterns have been highlighted that consist of four "lobes" separated vertically by the fiber and horizontally by the fracture, as shown in Fig. 11a, b. In order for the computer to label these lobes as a single object, they must first be joined. This is accomplished
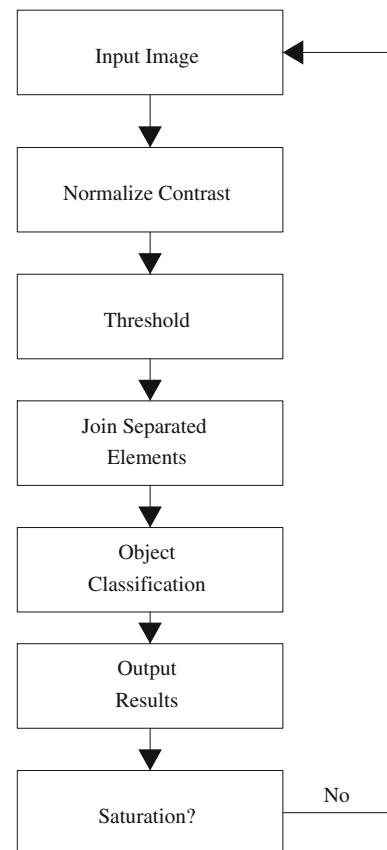

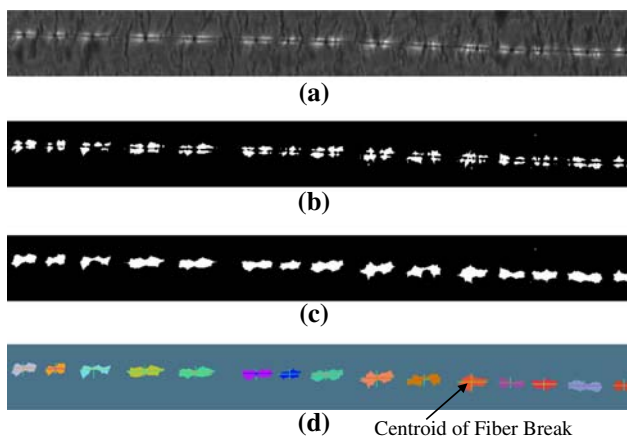**Fig. 10** Flowchart of the general break-finding algorithm

Fig. 11 Images of an **a** unprocessed, **b** thresholded, **c** closed, and **d** labeled and classified single fiber fragmentation specimen viewed under cross-polarized light. The crosses correspond to the coordinates of the centroid of the fiber break

by a series of dilations using a structuring element designed to expand the four lobes toward each other.

The highlighted objects are then labeled as separate and distinct by determining the connectivity of a given pixel to other pixels of the same value. The result is shown in Fig. 11c. The labeling is performed as a raster scan from the upper left corner of the image to the lower right, resulting in sequentially numbered regions. A false color mask is applied, giving each separate object a randomly assigned color for convenient viewing by the investigator.

Finally the objects are classified according to their calculated centroid, or center of mass. The coordinates of the centroid correspond closely to the coordinates of the fiber fracture. A portion of the resulting labeled and classified image is shown in Fig. 11d.

The procedure for the automated break search under normal lighting conditions is qualitatively similar to that for the birefringence search. Instead of thresholding to highlight bright regions such as birefringence patterns, dark regions are highlighted which constitute the breaks themselves. Since these regions are not separated into lobes as are the birefringence patterns, they do not require a series of dilations to become visible. They are slightly dilated, however, to render them easily visible to the user. The breaks manifest themselves as small rectangles (see Fig. 8), thus requiring a different structuring element for the dilation. The procedure to label and classify the breaks is identical to that for the birefringence.

Results and discussion

A glass/epoxy specimen subjected to incremental increases in stress showed characteristic stress–strain behavior, as

shown in Fig. 8. It is apparent that a large amount of plastic deformation was sustained. Because this experiment was performed under cross-polarized light, the algorithm designed to find birefringence patterns was used to count the fiber fragments.

The resulting fracture distribution is shown in Fig. 12, with each point representing a fracture and the locus of points representing the fiber. The fiber appears buckled because the ordinate axis is tremendously compressed, while the abscissa is expanded. Thus, the buckling of the fiber is on the order of 80 μm, but the average fragment length (the distance between points in Fig. 12) is on the order of 400 μm. Therefore, the fiber is slightly curved. In addition, the fiber is canted since precise placement of the fiber relative to the central axis of the silicone mold is difficult to accomplish manually. Therefore, the breaks locations in this figure are at a slight angle.

It is also apparent that some points were found that are not breaks. These errant breaks are caused primarily by defects in the specimen. In the present case, a bubble causes the errant breaks. Regardless of the cause of these errant breaks, they clearly do not fall on the locus of points that constitutes the fiber. The fragment distribution is therefore filtered to eliminate any points that do not lie within a given interval surrounding the fiber. Figure 13
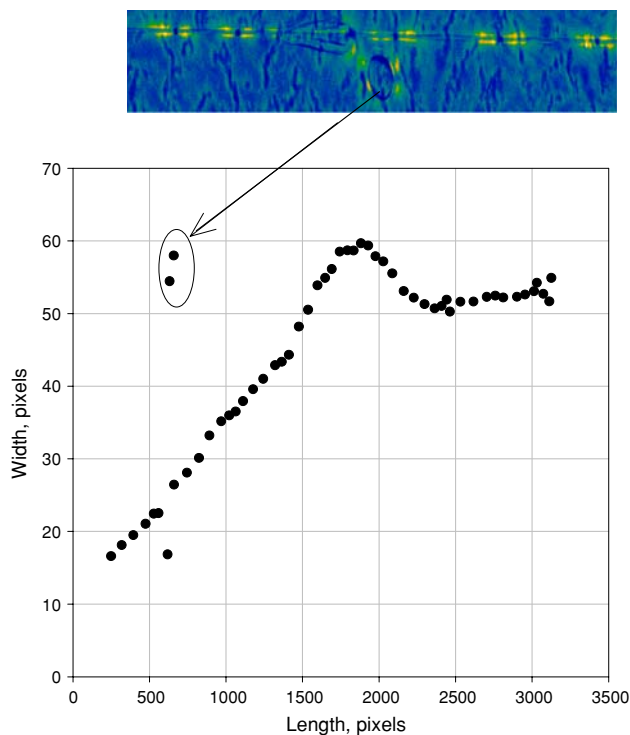

Fig. 12 Fiber fracture distribution for a specimen examined under cross-polarized light. Circled points are not actual breaks, but are caused by a bubble in the specimen as shown in the center of the accompanying image
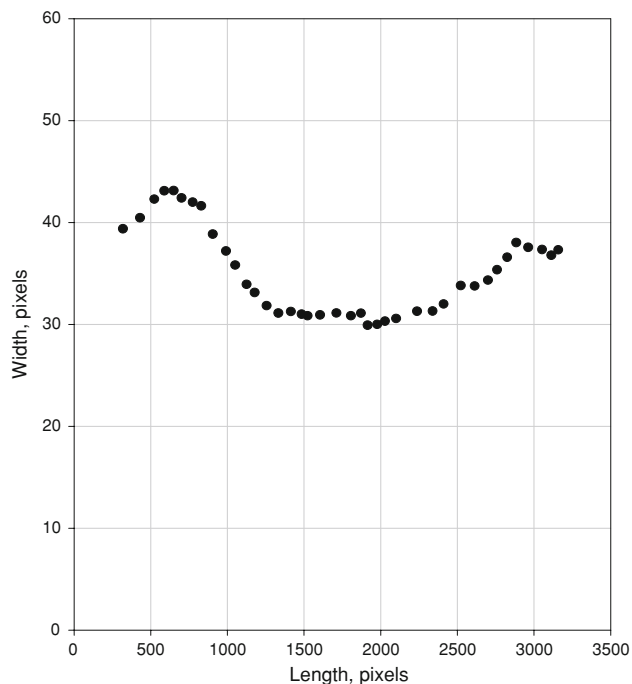
Fig. 13 Fiber fracture distribution for a specimen examined under normal lighting. This distribution has been filtered to remove false breaks

shows an example of a filtered fragment distribution obtained with the algorithm designed to find the breaks themselves. In this example, the fiber break locations are more horizontal, suggesting better placement of the fiber relative to the central axis of the silicone mold.

Table 1 summarizes a comparison between the results obtained for two specimens, one examined under cross-polarized light, and one examined under normal lighting

Table 1 Comparison of the experimental results for the current and earlier studies

Measurement	Number of breaks	Manual Ave. l_f (μm)	Centroid Ave. l_f (μm)	IFSS (MPa)[a]
#1	36(36)	496	496	
#2	39(39)	460	472	
#3	45(47)	394	378	
#4				
(a)	(33)	319		33.6
(b)	(36)	293		32.9
Ref [9]				44
Ref [9]		302		35.7
Ref [3]		443		52.4

[a] Interfacial shear strength in each study was calculated by Kelly-Tyson model and the critical fragment length at saturation was determined from the average fragment length by multiplying by 1.33

#3 was measured with birefringence under cross-polarized light

conditions. The break numbers in parentheses represent results of a manual counting method. Manual counting consists of clicking on the fiber fragment ends with a mouse (see expanded view of fiber break in Fig. 9). It is apparent that the number of breaks and the mean fragment lengths from each method are in close agreement. Small differences in the mean fragment length are evident because the automatic method calculates fragment length based on the centroid of each break, while the manual method requires the user to indicate the end of each fragment. The manually determined mean fragment length also reflects operator error attributable to the large number of fragments and the small size of the image on the computer screen.

Conclusions

Through the cooperative agreement with TRI, an automated IFSS testing apparatus has been developed that automatically strains the microcomposites, images the fiber of interest, automatically processes these images to obtain a measure of the IFSS, and provides archival capabilities to allow reanalysis of the experimental data as new data reduction methods are developed.

For the current autopeak detection and analysis programs, two algorithms were developed along with programmatic implementations of these algorithms. Prior knowledge of the failure mode is required before either of these algorithms can be implemented because they both depend on the assumption that either the breaks themselves, or birefringence caused by the stress fields surrounding the fiber fractures are visible.

Results obtained by both automated break-finding algorithms agree well with results found by a "point and click" method of break-finding. Furthermore, the analysis time is greatly reduced by using the automated algorithms. Analysis is performed on the order of seconds, whereas counting breaks with the mouse can take many minutes per image. It should be noted that both of these routines are much faster than the traditional method of examination under a microscope.

Results obtained directly from automated break-finding algorithms are highly dependent on the original condition of the specimens, since defects tend to manifest themselves as false breaks. This problem has been ameliorated somewhat by filtering the results to ignore points that do not fall on the locus of points that constitutes the fiber.

Finally, the automated IFSS instrument has been extend beyond its initial purpose to obtain archival images of fiber breaks and critical flaw nucleation in 2D multifiber microcomposites. This capability will be essential in investigating the factors that influence failure initiation in

composite structures. In addition, with the development of combinatorial microcomposites, the archival capabilities of this new machine should provide a basis for elucidating how fiber–fiber interactions influence IFSS. To fully exploit this new role, new algorithms must be developed that will allow the instrument to scan multiple regions during each dwell time between strain increments. In addition, new imaging techniques will be needed to allow depth profiling of the newly developed 3D multifiber arrays. At present, the instrument can perform only reliable analyses to 2D microcomposites. A Z-axis control is needed to look at 3D microcomposites. In the new design, changes would be made also to eliminate the defocusing that occurs in the current machine after 3 or 4 steps.

References

1. Holmes GA, Peterson RC, Hunston DL, McDonough WG, Schutte CL (2000) In: Schapery RA (ed) Time dependent and nonlinear effects in polymers and composites ASTM, p 98
2. Wagner HD, Steenbakkers LW (1989) J Mater Sci 24:3956. doi: 10.1007/BF01168959
3. van den Heuvel PWJ, Peijs T, Young RJ (2000) Composites Part A 31:165
4. van den Heuvel PWJ, Wubbolts MK, Young RJ, Peijs T (1998) Composites Part A 29:1121
5. van den Heuvel PWJ, Peijs T, Young RJ (1998) Compos Sci Technol 58:933
6. van den Heuvel PWJ, Peijs T, Young RJ (1997) Compos Sci Technol 57:899
7. van den Heuvel PWJ, Peijs T, Young RJ (1996) J Mater Sci Lett 15:1908
8. van den Heuvel PWJ, van der Bruggen YJW, Peijs T (1996) Composites Part A 27:855
9. Beyerlein IJ, Amer MS, Schadler LS, Phoenix SL (1998) Sci Eng Compos Mat 7:151
10. Li ZF, Grubb DT, Phoenix SL (1995) Compos Sci Technol 54:251
11. Li ZF, Grubb DT, Phoenix SL (1994) J Mater Sci 13:1720. doi: 10.1007/BF00451752
12. Favre JP, Auvray MH, CheneauHenry P, Galiotis C, Vlattas C, Paipetis A, Pegoraro M, Severini F, DiLandro L, Yuan LJ (1996) Polym Compos 17:937
13. Chohan V, Galiotis C (1997) Compos Sci Technol 57:1089
14. Holmes GA, McDonough WG (2002) In: Rasmussen BM, Pilato LA, Kliger HS (eds) Proceedings of the 47th international SAMPE symposium and exhibition—science of the advance materials and process engineering series. May 12, 47, p 1690
15. Holmes GA, Peterson RC, Hunston DL, McDonough WG (2007) Polym Compos 28:561